

## Optimizing the resolution of the alternating-gradient $m/\mu$ selector

Frank Filsinger, Stephan Putzke, Henrik Haak, Gerard Meijer,\* and Jochen Küpper  
*Fritz-Haber-Institut der Max-Planck-Gesellschaft, Faradayweg 4-6, D-14195 Berlin, Germany*

(Received 1 September 2010; published 15 November 2010)

We study the focusing of large neutral molecules in a molecular beam using electric fields. Since all quantum states of these molecules are high-field seeking under the practical experimental conditions, alternating gradient (AG) focusing has to be applied. The optimal ac frequency that yields the highest transmission depends on  $m/\mu$ , where  $\mu$  is the dipole moment and  $m$  denotes the mass. Therefore, an AG focuser can be used to select species with different  $m/\mu$  ratios, e.g., the conformers of neutral molecules [*Phys. Rev. Lett.* **100**, 133003 (2008)]. Here we demonstrate both theoretically and experimentally how the resolution of such an  $m/\mu$  selector can be optimized.

DOI: [10.1103/PhysRevA.82.052513](https://doi.org/10.1103/PhysRevA.82.052513)

PACS number(s): 33.15.-e, 37.20.+j

### I. INTRODUCTION

Experiments on the manipulation of gas-phase molecules with electric and magnetic fields have often been groundbreaking for chemistry and physics, from early deflection experiments that shed light on the quantum structure of atoms and molecules [1,2] to the development of coherent light sources [3] to recent cold-molecules experiments [4–6]. Until now, most experiments involving electric (and magnetic) fields were done on small molecules in low-field-seeking (lfs) quantum states. Molecules in such states, whose energy increases with increasing field strength, can relatively easily be focused and confined in space with static multipole fields [3,7]. However, extending these methods to large and more complex (bio-)molecules is challenging: For these species all quantum states are high-field seeking (hfs) at the relevant electric field strengths. Molecules in hfs states are intrinsically more difficult to manipulate as they have the tendency to crash into the electrodes, where the electric field is the highest. The situation is analogous to charged particle physics in that also ions cannot be confined with static potentials alone. Here the focusing problem was solved with the introduction of the AG principle [8,9]. The basic idea is to create an array of electrostatic lenses that focus the particles along one transverse coordinate while defocusing them along the perpendicular transverse axis. Alternating the orientation of these fields at the appropriate frequency results in a net focusing force along both transverse coordinates. This principle is exploited to confine ions in quadrupole mass filters [10,11], in Paul traps [10,12], and in virtually all particle accelerators. The application of AG focusing to neutral polar molecules was first proposed by Auerbach, Bromberg, and Wharton [13] and experimentally demonstrated by Kakati and Lainé for ammonia molecules in hfs states [14]. More recently, AG focusing was applied to the deceleration of polar molecules [15–18], to the guiding of cold molecules from an effusive source [19], and to the guiding of a supersonic jet of CaF molecules [20]. Furthermore, an  $m/\mu$  selector for neutral molecules, based on the AG principle, was implemented for the conformer separation of neutral molecules [21]. In a complementary approach it has been demonstrated recently that also static electric fields can be used

for the quantum-state selection [22] and conformer separation [23] of neutral molecules. Whereas this Stern-Gerlach type deflection method is technically easier to implement and offers an even better selectivity than the present  $m/\mu$  selector, it provides no focusing. Tightly focused molecular packages as obtained by an AG focuser, however, might be advantageous when also the detection laser beams need to be focused. This article demonstrates both theoretically and experimentally how the resolution of such an AG focuser can be optimized.

The article is structured as follows: After a brief discussion of the experimental setup in Sec. II, stability diagrams are introduced in Sec. III in order to illustrate the operation principle of the selector and to underline the conceptual analogy to the quadrupole mass filter for ions. In Sec. IV we present numerical simulations to support the focusing experiments on 4-aminobenzonitrile, shown in Sec. V. Finally, we summarize and conclude in Sec. VI.

### II. EXPERIMENTAL SETUP

The experimental setup, shown in Fig. 1(a), is similar to the one used for our previous experiments [21]. A sample of 4-aminobenzonitrile (ABN, Sigma-Aldrich, 98% purity) is heated to 110° C and coexpanded in 25 bar of neon through a pulsed Even-Lavie valve [24] into a vacuum. The valve has an orifice of 150  $\mu\text{m}$  and is operated at a repetition rate of 10 Hz. The mean velocity of the molecules in the beam is approximately 900 m/s with a velocity spread (full width at half maximum) of about 1%. After passing two skimmers, placed 15 and 25 cm downstream from the nozzle, the molecules enter a second, differentially pumped, vacuum chamber, in which the  $m/\mu$  selector is placed. The selector consists of four polished, 1-m-long, cylindrical stainless steel electrodes 4 mm in diameter. High voltages of 12 kV against ground are applied as shown in Fig. 1(b). Alternating gradient (AG) focusing is achieved by rapidly switching ( $<1 \mu\text{s}$ ) the voltages in a square wave between the two configurations that are depicted in Fig. 1. The transmitted ABN molecules are ionized 1.31 m downstream from the nozzle using one-color resonance-enhanced multiphoton ionization, (1 + 1) REMPI, via the  $S_1(v=0) \leftarrow S_0(v=0)$  transition at 299 nm [25]. The light is provided by a frequency-doubled pulsed dye laser (Radiant Dyes Narrowscan). The laser beam is unfocused and has a diameter of 3 mm and an energy of 1 mJ/pulse. Finally,

\*meijer@fhi-berlin.mpg.de

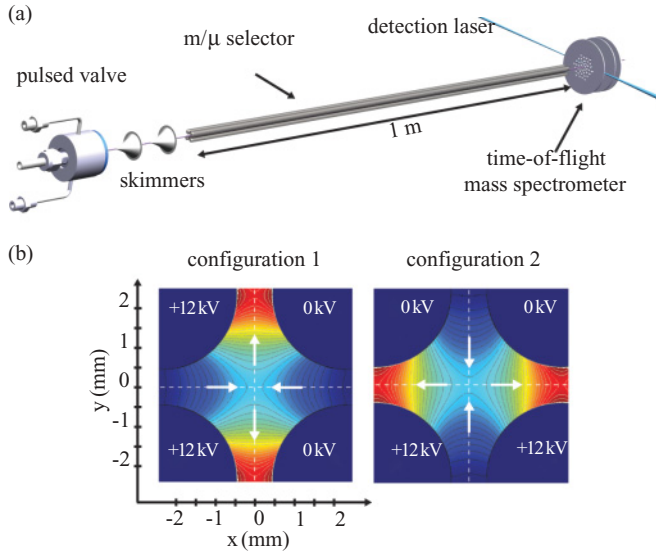


FIG. 1. (Color online) (a) Scheme of the experimental setup. (b) Cut through the high voltage electrodes and electric field configurations; red (gray) areas represent regions of strong electric field, blue (black) areas regions of weak electric field. The electric field strength at the center is 45 kV/cm and contour lines are given every 4 kV/cm. White arrows indicate the direction of the force experienced by molecules in high-field-seeking quantum states.

the ions are mass selectively detected in a linear time-of-flight mass spectrometer.

### III. OPERATION PRINCIPLE OF THE $m/\mu$ SELECTOR

In the AG focusing setup, shown in Fig. 1, the molecules traverse an array of alternating focusing and defocusing lenses. The array is created by switching between the two depicted field configurations, which interchanges focusing and defocusing directions. In each lens the force acting on a molecule increases with increasing distance from the molecular beam axis. As the molecules are on average further away from the molecular beam axis in a focusing lens compared to a defocusing lens, a net focusing effect results (provided, of course, that the focusing and defocusing forces at the same distance are of equal magnitude, which is fulfilled here in the central field region close to the molecular beam axis). Since the particle's motion is essential for efficient AG focusing, it is sometimes also referred to as “dynamic focusing.” The optimal switching frequency required for efficient focusing depends on the particle's dipole moment-to-mass ratio. If the voltages are switched too slowly the molecules are lost in the defocusing lens before they are refocused in the focusing lens. If the voltages are switched too rapidly, the molecules do not move enough for the restoring force to be bigger than the defocusing one and the time-averaged potential becomes flat. AG focusing works only for a finite range of frequencies, and for a given experimental geometry this range of frequencies depends on  $m/\mu$ .

The operation principle of the  $m/\mu$  selector is analogous to the separation of species based on their distinct charge-to-mass ratios in a quadrupole mass filter for ions. Most commercial quadrupole mass filters are driven by sinusoidal rf voltages that

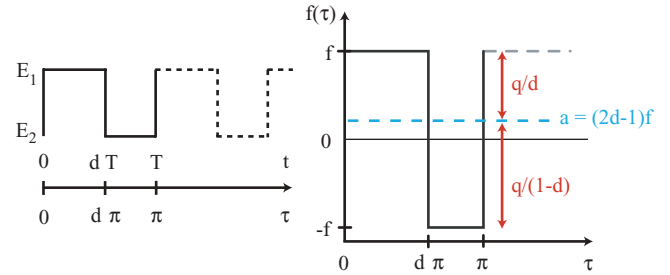


FIG. 2. (Color online) (Left) The electric field inside the selector is switched in a square wave pattern between two configurations  $E_1$  and  $E_2$ . The waveform with period  $T$  is  $\pi$  periodic in the dimensionless time  $\tau$ . (Right) Illustration of the parameters  $a$  and  $q$  that are used to describe the stability of the molecules' motion. See text for details.

are combined with a dc offset to optimize the  $m/q$  resolution. However, the rf waveform does not necessarily have to be sinusoidal. Richards *et al.* [26,27] pointed out, for instance, that a square wave can be used as well and that in this case the resolution can be optimized by changing the duty cycle, i.e., the relative duration of the waveform's two intervals of constant voltage (see Fig. 2). For technical reasons<sup>1</sup> this is also the approach that is implemented in our  $m/\mu$  selector. We will thus follow the theoretical description of the quadrupole mass filter with rectangular excitation introduced by Kononkov *et al.* [28] and Pipes [29].

Let us first derive the equations of motion for a polar molecule in the electric field of the selector, which is depicted in Fig. 1(b). The magnitude of the electric field in configuration (1) close to the molecular beam axis is, in a good approximation, given by

$$E(x, y) = E_0 + \eta(y^2 - x^2) \quad \text{with } \eta > 0. \quad (1)$$

For the sake of simplicity we assume that the molecule has a linear Stark shift. In this case the effective dipole moment  $\mu_{\text{eff}}$ , defined as the negative gradient of the potential energy with respect to the magnitude of the electric field, is constant and the Stark energy  $W_{\text{Stark}}$  can be written as

$$W_{\text{Stark}} = -\mu_{\text{eff}} E(x, y). \quad (2)$$

For high-field-seeking molecules with a positive  $\mu_{\text{eff}}$ , the configuration (1) shown in Fig. 1 represents a focusing lens in the  $x$  direction and a defocusing lens in the  $y$  direction. The equations of motion within this single lens are

$$\begin{aligned} m\ddot{x} &= -\frac{\partial W_{\text{Stark}}}{\partial x} = -2\mu_{\text{eff}}\eta x \\ m\ddot{y} &= -\frac{\partial W_{\text{Stark}}}{\partial y} = 2\mu_{\text{eff}}\eta y \end{aligned} \quad (3)$$

As shown in Fig. 2, the voltages are switched to configuration (2) after a time  $dT$ , where  $T$  is the period of the square

<sup>1</sup>High-voltage push-pull switches that are required to generate a square wave are readily available, whereas it is nontrivial to generate sine waves with an amplitude of 12 kV and variable frequency, even though we have set this up for other experiments in our laboratory [30].

wave with angular frequency  $\omega$  and  $d$ , which is in the range  $0 \leq d \leq 1$ , is called the duty cycle. In the most general case, the voltages used for the two configurations can be different and thus the two fields can be characterized by different parameters  $\eta_1$  and  $-\eta_2$ . Introducing the dimensionless time  $\tau = \omega t/2$  and the corresponding second derivative with respect to time, the equations of motion can be written as

$$\begin{aligned} \frac{d^2x}{d\tau^2} + \frac{8\mu_{\text{eff}}\eta(\tau)}{m\omega^2}x &= 0 \\ \frac{d^2y}{d\tau^2} - \frac{8\mu_{\text{eff}}\eta(\tau)}{m\omega^2}y &= 0 \end{aligned}, \quad \eta(\tau) = \begin{cases} \eta_1 & \text{for } 0 < \tau \leq d\pi \\ -\eta_2 & \text{for } d\pi < \tau < \pi \end{cases} \quad (4)$$

Eq. (4) takes the form of Hill's differential equation:

$$\frac{d^2u}{d\tau^2} + f_u(\tau)u(\tau) = 0, \quad u = x, y, \quad (5)$$

where  $f_u(\tau) = f_u(\tau + \pi)$  is a  $\pi$ -periodic function in the dimensionless time  $\tau$ . In order to solve Eq. (5) we follow the approach of Kononov *et al.* [28] and Pipes [29] using matrix methods: If  $u_A(\tau)$  and  $u_B(\tau)$  are two linearly independent solutions of Eq. (5) defined by the initial conditions

$$\begin{aligned} u_A(0) &= 1 & u_B(0) &= 0 \\ u'_A(0) &= 0 & u'_B(0) &= 1, \end{aligned} \quad (6)$$

then the general solution  $u(\tau)$  can be written as a linear superposition of these two solutions:

$$u(\tau) = u_0u_A(\tau) + v_{0,u}u_B(\tau), \quad (7)$$

where the initial conditions are given by  $u(0) = u_0, u'(0) = v_{0,u}$ . At the end of the first switching period, i.e., for  $\tau = \pi$ , the initial phase-space position for the next switching period is reached:

$$u(\pi) = u_0u_A(\pi) + v_{0,u}u_B(\pi) =: u_1 \quad (8)$$

$$u'(\pi) = u_0u'_A(\pi) + v_{0,u}u'_B(\pi) =: v_{1,u}. \quad (9)$$

Because  $u_A(\tau)$  and  $u_B(\tau)$  are  $\pi$ -periodic functions, at time  $\tau$  in the second period, i.e., for  $\pi < \tau < 2\pi$ , the same solutions  $u_A$  and  $u_B$  are valid, and the following equations are obtained:

$$u(\tau) = u_1u_A(\theta) + v_{1,u}u_B(\theta) \quad (10)$$

$$u'(\tau) = u_1u'_A(\theta) + v_{1,u}u'_B(\theta), \quad (11)$$

with  $\theta = \tau - \pi$ . This procedure can be iteratively repeated and finally in the  $(n+1)$ th period, for  $n\pi < \tau < (n+1)\pi$  and  $\theta = \tau - n\pi$ , we obtain:

$$u(\tau) = u_nu_A(\theta) + v_{n,u}u_B(\theta) \quad (12)$$

$$u'(\tau) = u_nu'_A(\theta) + v_{n,u}u'_B(\theta) \quad (13)$$

This representation of the solution  $u(\tau)$  is called a *state vector* representation and can be written in matrix form:

$$\begin{pmatrix} u_{n+1} \\ v_{n+1,u} \end{pmatrix} = M_u \begin{pmatrix} u_n \\ v_{n,u} \end{pmatrix} = M_u^{n+1} \begin{pmatrix} u_0 \\ v_{0,u} \end{pmatrix} \quad (14)$$

with

$$M_u = \begin{bmatrix} u_A(\pi) & u_B(\pi) \\ u'_A(\pi) & u'_B(\pi) \end{bmatrix} = \begin{bmatrix} m_{11} & m_{12} \\ m_{21} & m_{22} \end{bmatrix} \quad (15)$$

$M_u$  is called the transfer matrix and can be used to calculate a particle's phase-space position at any time  $\tau$  from the initial phase-space position at time  $\tau = 0$ . The trace of  $M_u$  determines the stability of the solution. Whereas the amplitude of the particle motion increases exponentially for  $|\text{Tr}(M_u)| \geq 2$ , stable trajectories exist for [29]

$$-2 < \text{Tr}(M_u) < 2. \quad (16)$$

Using the transfer matrix formalism, the problem of solving the equations of motion is reduced to determining the pair of linearly independent solutions  $u_A$  and  $u_B$  during one period  $0 < \tau < \pi$  and the subsequent iterative calculation of the state vectors.

If the waveform consists of subintervals during which the function  $f_u(\tau) = f$  is constant, Eq. (5) can be solved analytically [28]. Two cases depending on the sign of  $f$  need to be distinguished. For  $f > 0$  (corresponding to a focusing lens) the solution is

$$u(\tau) = u_s \cos[(\tau - \tau_s)\sqrt{f}] + \frac{v_s}{\sqrt{f}} \sin[(\tau - \tau_s)\sqrt{f}]. \quad (17)$$

Here  $u_s$  and  $v_s$  denote the particle's position and velocity at the beginning of the respective subinterval at time  $\tau_s$ . The transfer matrix  $F(f, \Delta)$  for the focusing lens is obtained by evaluating  $u(\tau_e)$ , where  $\tau_e$  is the time corresponding to the end of the subinterval and  $\Delta = \tau_e - \tau_s$ .

$$F(f, \Delta) = \begin{bmatrix} \cos(\Delta\sqrt{f}) & \frac{1}{\sqrt{f}} \sin(\Delta\sqrt{f}) \\ -\sqrt{f} \sin(\Delta\sqrt{f}) & \cos(\Delta\sqrt{f}) \end{bmatrix}. \quad (18)$$

For a subinterval with  $f < 0$  (corresponding to a defocusing lens) the solution of Eq. (5) is

$$u(\tau) = u_s \cosh[(\tau - \tau_s)\sqrt{-f}] + \frac{v_s}{\sqrt{-f}} \sinh[(\tau - \tau_s)\sqrt{-f}], \quad (19)$$

and the transfer matrix  $D(f, \Delta)$  for the defocusing lens is

$$D(f, \Delta) = \begin{bmatrix} \cosh(\Delta\sqrt{-f}) & \frac{1}{\sqrt{-f}} \sinh(\Delta\sqrt{-f}) \\ \sqrt{-f} \sinh(\Delta\sqrt{-f}) & \cosh(\Delta\sqrt{-f}) \end{bmatrix}. \quad (20)$$

In the case of the  $m/\mu$  selector the waveform consists of two subintervals of duration  $\Delta_1 = \pi d$  and  $\Delta_2 = \pi(1-d)$ . During these two intervals the function  $f_x$  for the  $x$  coordinate takes the values  $f_1$  and  $f_2$ , respectively, with

$$f_1 = \frac{8\mu_{\text{eff}}\eta_1}{m\omega^2} \quad \text{and} \quad f_2 = -\frac{8\mu_{\text{eff}}\eta_2}{m\omega^2}. \quad (21)$$

From Eq. (4) we see that the corresponding function  $f_y$  for the motion along the  $y$  coordinate equals  $-f_x$ . The transfer matrices  $M_x$  and  $M_y$  for the complete period are obtained by multiplying the transfer matrices of the subintervals:

$$\begin{aligned} M_x &= D(f_2, \Delta_2) \times F(f_1, \Delta_1) \\ M_y &= F(-f_2, \Delta_2) \times D(-f_1, \Delta_1). \end{aligned} \quad (22)$$

Note that this method can be applied not only to square waves but also to arbitrary periodic waveforms by subdividing these smooth waveforms into sufficiently small intervals of constant voltage [29]. By evaluating the trace of the transfer matrices

$M_x$  and  $M_y$  according to Eq. (16), stable operation conditions, depending on the three independent parameters  $f_1$ ,  $f_2$ , and  $d$ , can be found.

In order to characterize the quadrupole mass filter for ions, however, usually two different parameters  $a$  and  $q$  are used. These parameters are related to the dc and rf amplitudes, respectively. While  $a$  describes the average force constant over one rf period,  $q$  corresponds to the change of the force constant during one period. The stability of the solutions of the equation of motion solely depends on the values of  $a$  and  $q$ . Therefore, often  $a$ - $q$  maps are drawn to visualize stable operation conditions and to illustrate the operation principle of the device [10,11]. Such stability diagrams have also been introduced to describe the trapping of ammonia in an ac trap for neutral molecules [31] and shall be discussed here in the context of the  $m/\mu$  selector. Analogous to the definition of  $a$  and  $q$  in the case of the quadrupole mass filter, these parameters can be introduced for the  $m/\mu$  selector:

$$\begin{aligned} a &:= a_x = -a_y = d f_1 + (1-d) f_2 \\ q &:= q_x = -q_y = (f_1 - f_2) d (1-d). \end{aligned} \quad (23)$$

The transfer matrices can then be expressed in terms of  $a$ ,  $q$ , and  $d$ :

$$\begin{aligned} M_x &= D\left(a - \frac{q}{1-d}, \Delta_2\right) \times F\left(a + \frac{q}{d}, \Delta_1\right) \\ M_y &= F\left(-a + \frac{q}{1-d}, \Delta_2\right) \times D\left(-a - \frac{q}{d}, \Delta_1\right). \end{aligned} \quad (24)$$

The stability diagrams, shown in Fig. 3 for  $d = 0.50$  and  $d = 0.40$ , are obtained by evaluating the traces of  $M_x$  and  $M_y$  according to Eq. (16). Dark gray areas indicate parameters where the motion along  $x$  is stable, whereas light gray areas indicate stable areas for the  $y$  coordinate. Only in the black areas, where both stability conditions are fulfilled, stable trajectories are obtained. The regions of stable parameters

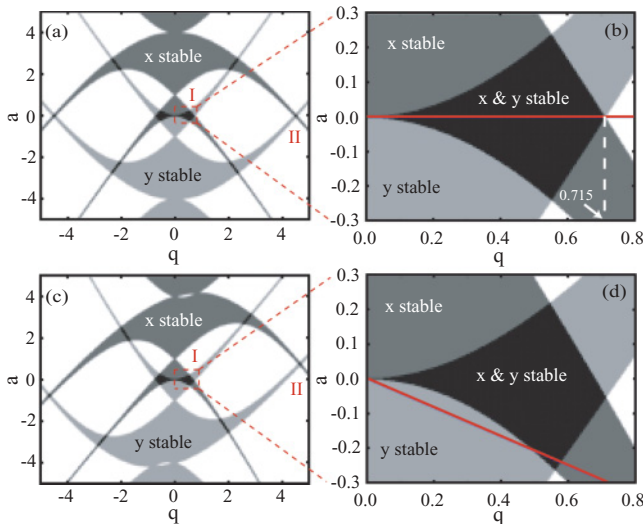


FIG. 3. (Color online)  $a$ - $q$  maps for  $d = 0.5$  (top) and  $d = 0.4$  (bottom). The right-hand side shows the first stable region on an enlarged scale. Work lines, corresponding to ac frequency scans, are drawn as solid red lines; see text for details.

along both axes are symmetric with respect to a reflection about the  $q = 0$  line for  $d = 0.50$ . For all duty cycles the stable regions are point symmetric about the origin. At constant  $\omega$ ,  $d$ , and  $\eta$ , a given  $m/\mu_{\text{eff}}$  ratio corresponds to a specific operating point  $(q, a)$  in the stability diagram. For technical reasons, the present selector is switched between two configurations of equal electric field strength [i.e., with  $|\eta_1| = |\eta_2|$ ; see Eq. (4)]. Therefore,  $f_1$  and  $f_2$  are also of the same magnitude  $f$  and differ only by their sign. Figure 2 illustrates the waveform applied to the selector and the meaning of  $a$  and  $q$ . For a duty cycle of 0.5, the average  $a$  is always zero and the amplitude of the waveform is given by  $2q$ . If the duty cycle differs from 0.5,  $a$  is nonzero and  $q$  characterizes the change of  $f$  on switching relative to the average value  $a$ . The ratio  $a/q$  is constant, independent from  $m/\mu_{\text{eff}}$ , and depends only on the duty cycle. Therefore, all work points in the stability diagram lie along a straight line through the origin with slope  $s$ ,

$$s = \frac{2d - 1}{2d(1 - d)} \quad (25)$$

and the actual range of  $m/\mu_{\text{eff}}$  ratios that are transmitted can be scanned by changing the ac frequency. Figures 3(b) and 3(d) shows stability diagrams for  $d = 0.50$  and  $d = 0.40$  together with the work lines on an enlarged scale. For  $d = 0.50$  [Fig. 3(b)] stable trajectories are obtained for  $q < 0.715$  and  $4.47 < q < 4.54$ . Thus, all species with a  $m/\mu_{\text{eff}}$  ratio in the ranges

$$0 > \frac{m}{\mu_{\text{eff}}} > \frac{4\eta}{0.715\omega^2} \quad \text{or} \quad \frac{4\eta}{4.47\omega^2} > \frac{m}{\mu_{\text{eff}}} > \frac{4\eta}{4.54\omega^2} \quad (26)$$

are transmitted. The  $m/\mu_{\text{eff}}$  resolution of the selector can be increased by operating the device at a duty cycle that differs from 0.50. Now the work line is tilted away from the  $a = 0$  line and cuts through the tip of the stable region as shown for  $d = 0.40$  in Fig. 3(d). Therefore, only species within a much narrower range of  $m/\mu_{\text{eff}}$  ratios are transmitted.

The stability diagrams for duty cycles larger than 0.50 are obtained by reflecting the stability diagrams (and the work lines) for  $d < 0.50$  and the same  $\Delta d = |d - 0.5|$  about the  $a = 0$  line. Note that the second, narrow region around  $q = 4.5$  that is stable for  $d = 0.50$  [Fig. 3(a)], is not sampled when tuning the duty cycle away from 0.50. For  $d < 0.50$  this region shifts upward into the upper half plane of the  $a$ - $q$  diagram, whereas the work line has a negative slope and only values in the lower half plane are sampled (*vide supra*). For  $d > 0.50$  the situation is analogous, i.e., the second stable region is shifted downward and the work line covers only the upper half plane of the  $a$ - $q$  map.

While it is instructive to describe the operation principle of the selector using the same parameters  $a$  and  $q$  that are typically used for the quadrupole mass filter, it is at the same time somewhat cumbersome to draw a new stability diagram for each duty cycle. In the current operation mode, where the magnitude of the voltages is the same for the focusing and the defocusing lenses, the parameters  $a$  and  $q$  cannot be varied independently. For this special case it is more convenient to draw an  $f$ - $d$  map to visualize stable operation conditions as shown in Fig. 4. Here, all work lines, corresponding to sweeping the ac frequency for a fixed duty cycle, are vertical

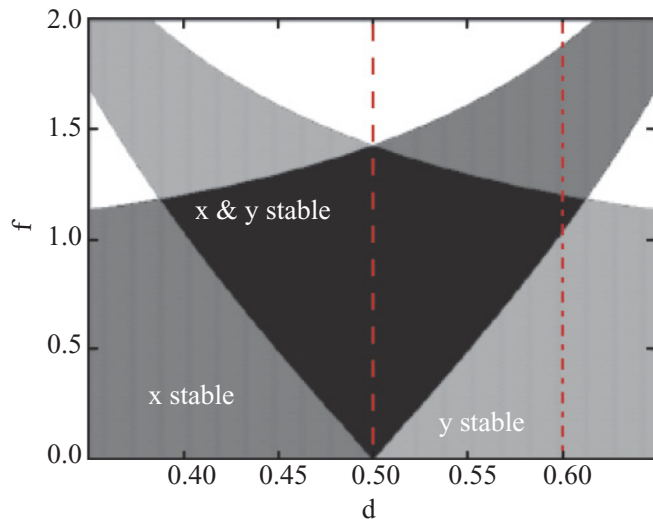


FIG. 4. (Color online) Stability diagram for the  $m/\mu$  selector. The region where the motion along both transverse coordinates is stable is indicated by the black area. Work lines in the current operation mode (sweeping the ac frequency) correspond to vertical lines.

and only one stability diagram suffices to describe the device. From this diagram it is seen that stable operation conditions exist for  $0.38 < d < 0.62$ .

We can conclude that changing the duty cycle of the  $m/\mu$  selector increases its resolution just as it does for the ion guide with rectangular excitation. It has the same effect as adding a dc offset to the rf potential in the commonly used quadrupole mass filter for ions with sinusoidal waveforms. However, in order to compare the conclusion drawn from the stability diagrams to real experiments, several points have to be considered. First, the stable areas in the  $a-q$  and  $f-d$  maps indicate operation conditions, where the amplitude of the particle's motion remains finite, but this amplitude may be too large for the molecule to pass through the device. A molecule is lost once the amplitude of its motion becomes larger than the mechanical aperture of the selector. Second, particles whose trajectories are unstable in an infinitely long selector might in practice still reach the detection area on

metastable trajectories, if the increase of their amplitude is slow compared to the time of flight through the selector. For quadrupole mass filters, it has been shown that 25 cycles are not enough to remove all ions on unstable trajectories from the beam [32]. In the present work, with typical switching frequencies of 2–8 kHz, the molecules spend 1–2 ms in the selector and, therefore, they typically experience 10 switching cycles. Thus, it is expected that indeed particles on metastable trajectories are present in the detection region. Third, the electric field as given in Eq. (1) is only a good approximation for a small region around the molecular beam axis. In order to realistically describe the field of the selector, either higher order terms have to be taken into account or a numerically calculated field has to be used. Finally, the assumption that the Stark effect is linear may be valid for symmetric tops and certain small molecules, but it is not a good approximation for large asymmetric tops in rotationally excited states, where  $\mu_{\text{eff}}$  often varies strongly with the electric field strength. Therefore, numerical simulations, as described in the following section, are performed to support the experimental data.

#### IV. NUMERICAL DESCRIPTION

In order to simulate the propagation of an ensemble of molecules through the selector, the electric field is calculated with finite-elements methods (COMSOL Multiphysics) and trajectory calculations are performed using the home-built software package LIBCOLDMOL [33]. Details on these calculations and on the modeling of a molecular beam are given in Ref. [34]. To demonstrate the quantum-state selectivity of the selector, simulations are performed for three  $J_{K_a K_c} M$  states of ABN. The three states that are chosen for the simulations represent three prototypical cases for the rotational states of complex asymmetric top molecules, and their Stark shifts and effective dipole moments are shown in Fig. 6. These Stark curves generally show neither a linear nor a quadratic behavior, which would be expected for simple perturbative first- or second-order interactions. Even though there is no first-order interaction between the eigenstates of these asymmetric top molecules, the lowest rotational quantum states have nearly linear Stark curves at the relevant electric field strengths. The

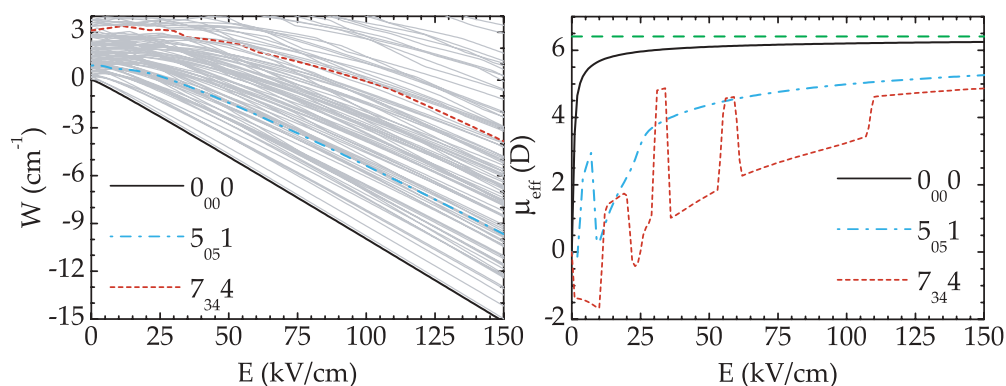


FIG. 5. (Color online) (Left) Potential energy as a function of the electric field strength for the lowest rotational quantum states of 4-aminobenzonitrile. The three  $J_{K_a K_c} M$  states, for which the simulations shown in Fig. 5 have been performed, are highlighted. (Right) Effective dipole moment as a function of the electric field strength for the states highlighted in the left graph. The value of the permanent dipole moment of 4-aminobenzonitrile is indicated by the green dashed line.

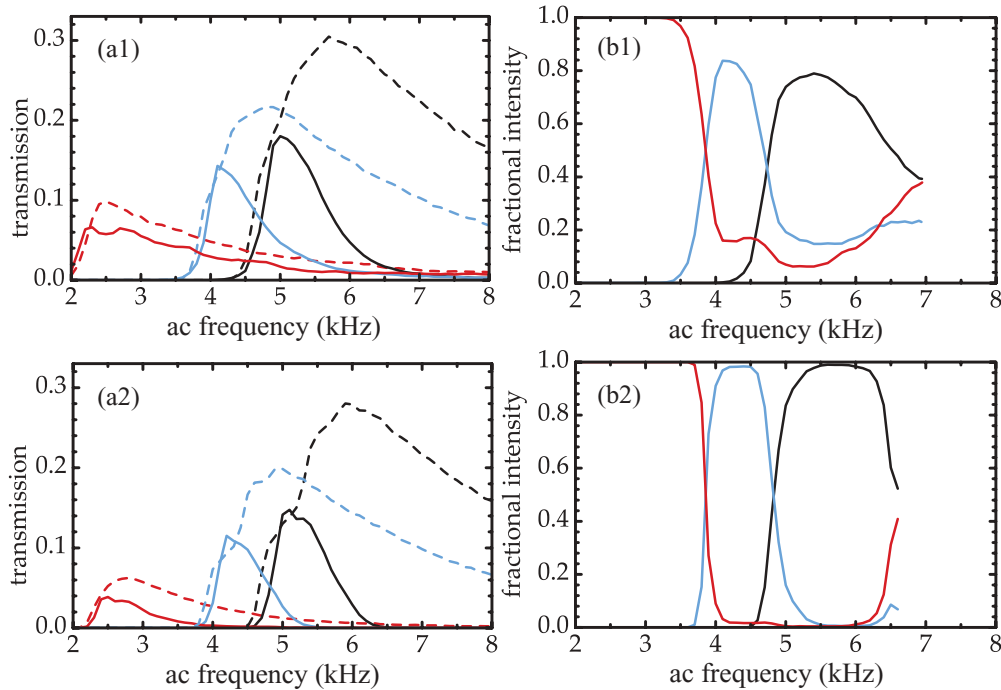


FIG. 6. (Color online) (Left) Simulated transmission of 4-aminobenzonitrile molecules seeded in Ne through the present setup (a1) and a 2-m-long selector (a2), for  $d = 0.50$  (dashed lines) and  $d = 0.58$  (solid lines). Black curves correspond to molecules in the  $J_{K_a K_c} M = 0_{00}0$  rotational state, blue (light gray) and red (dark gray) curves are obtained for  $J_{K_a K_c} M = 5_{05}1$  and  $J_{K_a K_c} M = 7_{34}4$ , respectively. (Right) Fractional intensities of individual states for  $d = 0.58$  as a function of the ac frequency. Graph (b1) is calculated for the present setup; (b2) is calculated for a 2-m-long selector. See text for details.

rotational ground state ( $J_{K_a K_c} M = 0_{00}0$ ), which has the largest effective dipole moment and no avoided crossings, can be seen as a prototype for such low rotational states. The  $5_{05}1$  state represents an intermediate quantum state whose Stark curve has some avoided crossings at relatively weak electric fields and becomes smooth at strong fields. Its average  $\mu_{\text{eff}}$  equals  $2/3$  of the ground-state  $\mu_{\text{eff}}$ . Finally, the  $7_{34}4$  state is a typical example for high-lying rotational states exhibiting many avoided crossings distributed over the relevant field strength region. Its effective dipole moment, which strongly varies with the field strength, has an average value amounting to 40% of that of the ground state. For the simulations shown in this section, equal initial populations of the states are assumed.

Figure 6(a1) shows the simulated transmission through the present setup, i.e., the fraction of the molecules passing the skimmer that reach the detection region, as a function of the ac frequency for  $d = 0.50$  (dashed lines) and  $d = 0.58$  (solid lines). The transmission curves for  $d = 0.50$  all have a similar shape with a sharp cutoff at the low-frequency side of the transmission maximum and a long “tail” at high frequencies. However, the transmission curves for the individual states are shifted with respect to each other and, depending on the chosen frequency, a specific state can be preferentially selected. At frequencies above 5 kHz the state with the largest  $\mu_{\text{eff}}$  is selected (here the  $0_{00}0$  state). In the frequency range between 3.75 and 5 kHz the transmission of the  $5_{05}1$  state with the intermediate  $\mu_{\text{eff}}$  is enhanced. The only state which can be completely isolated is the least polar  $7_{34}4$  state, which has the smallest effective dipole moment.

Changing the duty cycle from  $d = 0.50$  to  $d = 0.58$  clearly changes the shape of the transmission curves and reduces the maximum intensities for all three quantum states. The reduction of the transmission is most pronounced at the high-frequency sides of the transmission curves, whereas the intensity stays approximately constant near the low-frequency cutoff. Because the widths of the transmission curves become much narrower and the low-frequency cutoffs occur at the same ac frequency, the  $m/\mu_{\text{eff}}$  resolution is clearly improved for  $d = 0.58$ . To quantify the improved quantum-state selectivity, Fig. 6(b1) depicts the fractional intensity, which is obtained by dividing the transmission curve of a given species by the sum of the transmission curves for all species for  $d = 0.58$ . For this duty cycle and the present experimental setup, the maximum fractional intensity is 79% for  $J_{K_a K_c} M = 0_{00}0$ , 84% for  $J_{K_a K_c} M = 5_{05}1$ , and 100% for  $J_{K_a K_c} M = 7_{34}4$  (assuming that only these three states are present initially). This imperfect selectivity is mainly caused by the remaining long “tails” of the transmission curves for the less polar species. For the 1-m-long selector and an expansion in Ne, resulting in a mean velocity of 900 m/s, many molecules are transmitted on metastable trajectories due to the low number of switching cycles that the molecules experience. This is particularly true for the  $7_{34}4$  state, which only interacts weakly with the electric field. Doubling the number of switching cycles by doubling the length of the selector significantly suppresses this transmission at high frequencies, as shown in Fig. 6(a2). For this 2-m-long setup, a clearly improved selectivity is predicted with a quantum-state purity  $\geq 98\%$  for all three states [see Fig. 6(b2)].

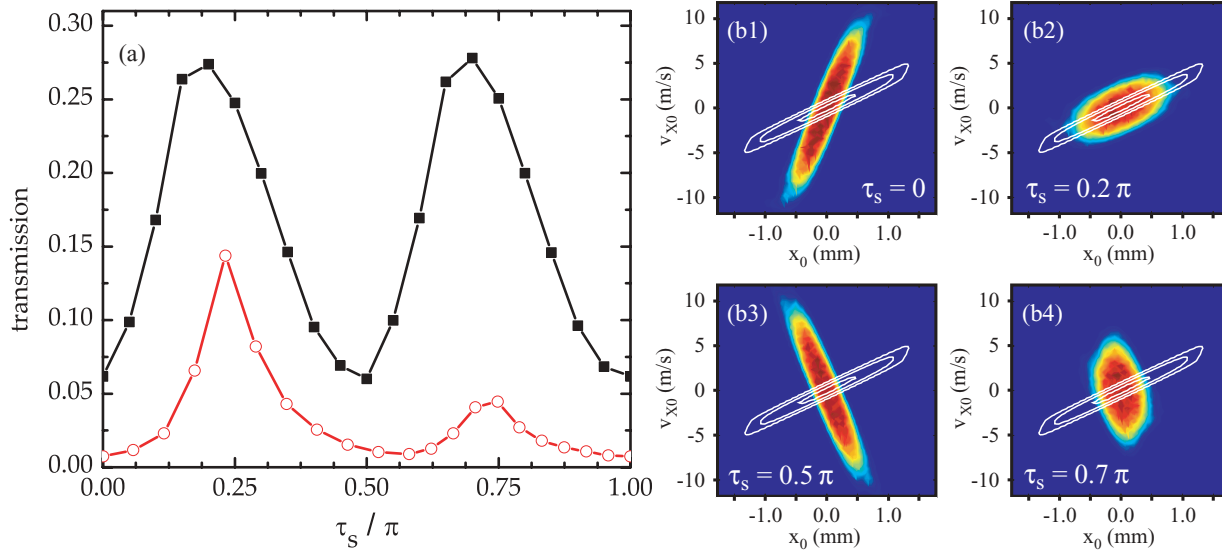


FIG. 7. (Color online) (a) Simulated transmission through a 2-m-long selector as a function of the start phase for 4-aminobenzonitrile molecules in the rotational ground state. Calculations for  $d = 0.50$  ( $d = 0.58$ ) and an ac frequency of 6.0 kHz (5.0 kHz)—the maximum of the respective transmission curves—are shown as squares (circles). (b1)–(b4) Relative probability for a molecule to be accepted as a function of the initial phase-space position in the  $x_0$ - $v_{x0}$  plane, for different start phases, an ac frequency of 6.0 kHz, and  $d = 0.50$ . The acceptance probability increases from the blue (black) areas toward the red (dark gray) areas. The white contour lines show the emittance of the source, i.e., the relative probability to find a molecule at  $(x_0, v_{x0})$  under the present experimental conditions. Contour lines are given for values of 0.1, 0.5, and 0.9.

For a given ac frequency the transmission through the selector depends on the start phase  $\tau_s$  of the switching cycle. As we have described the waveform using the  $\pi$ -periodic function  $f(\tau)$  [see Eq. (4) and Fig. 2] we will keep this notation here, i.e.,  $\tau_s \in [0, \pi]$ . Two equally good start phases exist for  $d = 0.50$  as shown by the black curve in Fig. 7(a). The optimal start phase is determined by the overlap between the phase-space distribution of the molecules at the entrance of the selector (i.e., the *emittance* of the source) and the accepted volume of the phase space. Figures 7(b1)–7(b4) illustrate that this overlap depends on  $\tau_s$ . The color-coded images show the probability for a molecule to be accepted by the selector depending on its initial position in the  $x$ - $v_x$  plane ( $x_0, v_{x0}$ ). To obtain these images,  $10^8$  molecules that are uniformly distributed in phase space at the entrance of the selector are propagated for 150 switching cycles. This large number of cycles ensures that molecules on metastable trajectories are removed and only molecules on stable trajectories are taken into account. Figures 7(b1)–7(b4) then show the relative probability for an accepted molecule to have started at  $(x_0, v_{x0})$  on a linear color scale. This relative probability is not uniform since the motions along  $x$  and  $y$  are coupled by higher-order terms in the multipole expansion of the focusing potential. Whereas the total acceptance of the selector, i.e., the integrated intensity in Figs. 7(b1)–7(b4), is independent from the start phase, the fraction of the phase space that is accepted is not. Because the emittance of the source, which is indicated as contour lines in Figs. 7(b1)–7(b4), solely depends on the experimental conditions and not on the start phase, a  $\tau_s$ -dependent transmission results. The best overlap in the  $x$ - $v_x$  plane between accepted area and the emittance is obtained for  $\tau_s = 0.2\pi$  [see Fig. 7(b2)]. Since the applied waveform

is symmetric with respect to  $x$  and  $y$  focusing for  $d = 0.50$ , the respective images for the  $y$ - $v_y$  plane and  $\tau_s$  equal those for the  $x$ - $v_x$  plane and  $\tau_s + 0.5\pi$ . Thus for the  $y$  coordinate  $\tau_s = 0.7\pi$  is optimal. The transmission through the selector is determined by the product of the overlapping areas in the  $x$ - $v_x$  and  $y$ - $v_y$  planes. It is the same for  $\tau_s = 0.2\pi$  and  $\tau_s = 0.7\pi$  and, therefore, these two start phases yield identical intensities.

For  $d \neq 0.50$  the symmetry of the waveform is broken and starting with  $x$  or  $y$  focusing is not equivalent anymore. The same arguments regarding the overlap between the accepted phase space area and the emittance can be made, and the respective plots for  $d = 0.58$  are shown in Fig. 8. As demonstrated in Fig. 7(a) for  $d = 0.58$ , starting with  $x$  focusing is favorable for  $d > 0.50$ , i.e., when the focusing interval along  $x$  is longer than the focusing interval along  $y$ . For  $d < 0.50$  the situation is reversed and starting with  $y$  focusing is favored.

## V. EXPERIMENTAL RESULTS

In order to experimentally demonstrate the effect of the duty cycle, studies on ABN are performed. ABN is chosen because it has a very favorable  $m/\mu$  ratio for AG focusing (mass 118 u,  $\mu = 6.41$  D [35]) and possesses a sufficiently high density of rotational states. This high density of states is an important characteristic when the potential of the  $m/\mu$  selector is to be estimated. Due to the high density of states, many high- $J$  states that generally have a small  $\mu_{\text{eff}}$  are populated even at the low temperatures in a molecular beam. At a rotational temperature of 1 K, for instance, a temperature that can routinely be achieved with an Even-Lavie valve, the relative populations of the  $5_{051}$  and  $7_{344}$  states with respect to the ground state are 54 and 3%, respectively. For such a cold beam only a very

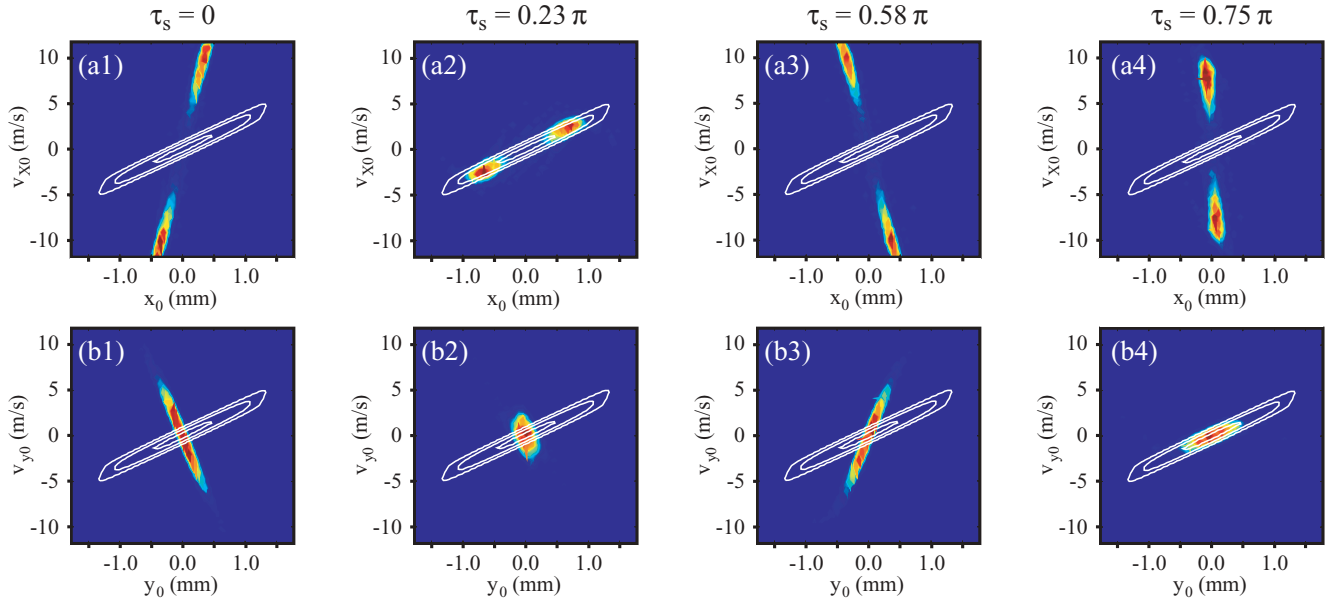


FIG. 8. (Color online) Relative probabilities for a molecule to be accepted as a function of its initial phase-space position in the  $x_0$ - $v_{x_0}$  plane (a1)–(a4) and the  $y_0$ - $v_{y_0}$  plane (b1)–(b4). The different start phases are indicated in the figure and the color coding represents the transmission. The acceptance probability increases from the blue (black) areas toward the red (dark grey) areas. To obtain the images,  $10^8$  molecules are propagated for 125 switching cycles at an ac frequency of 5.0 kHz and  $d = 0.58$ . The white contour lines show the relative probability to find a molecule at  $(x_0, v_{x_0})$  under the present experimental conditions. Contour lines are given for values of 0.1, 0.5, and 0.9.

small transmission at low ac frequencies is expected, consistent with the large value of ABNs permanent dipole moment. At 4 K, a rotational temperature typical for the previously used General Valve Series 99 valve however, the populations relative to the ground state are already 144% for  $J_{K_a K_c} M = 5_{05}1$  and 84% for  $J_{K_a K_c} M = 7_{34}4$ . These large populations of relatively high- $J$  states would cause a significant transmission at low ac frequencies. In conformer-selection experiments this may cause unwanted background signal, similar to what was observed for 3-aminophenol [21], and reduce the contrast.

Figure 9 shows the intensity of the focused molecular beam of ABN, normalized to the intensity of the free jet, as a function of the ac frequency for different duty cycles  $d \geq 0.49$ . Each data point was recorded in 80 s and thus a complete transmission curve was obtained within  $\sim 1$  h. As shown in Fig. 7, the start phase of the switching sequence is crucial for the overall transmission through the selector. However, the end phase is also important because it determines the shape of the molecular packet in the detection region and, therefore, the overlap between the detection laser and the target molecules [36]. Even though an unfocused laser beam is used here to minimize this effect, spatial inhomogeneities in the laser beam profile still result in a residual end-phase-dependent detection efficiency. For a given ac frequency, the start and end phases cannot be varied independently. As it is not *a priori* clear which start phase yields the highest signal, we experimentally determined the optimal start phase for each ac frequency to obtain the transmission curves shown in Fig. 9. The transmission curves for  $d = 0.49$  and  $d = 0.50$  are comparable both in width and peak intensity. As the duty cycle is increased, the peak intensities and the width of the

transmission curves both decrease, with the largest decrease in intensity at the high-frequency side of the maximum. While the high-frequency cutoff clearly shifts to smaller frequencies with increasing duty cycle, the peak position and the low-frequency cutoff occur approximately at the same position for all duty cycles. As a consequence, the separation of ABN from a second species with different  $m/\mu$  ratio would be clearly improved when operating the selector at  $d \neq 0.50$ . We can thus conclude that the selectivity indeed improves at the cost of a reduced overall transmission, as theoretically expected from matrix theory (Sec. III) and the numerical simulations (Sec. IV).

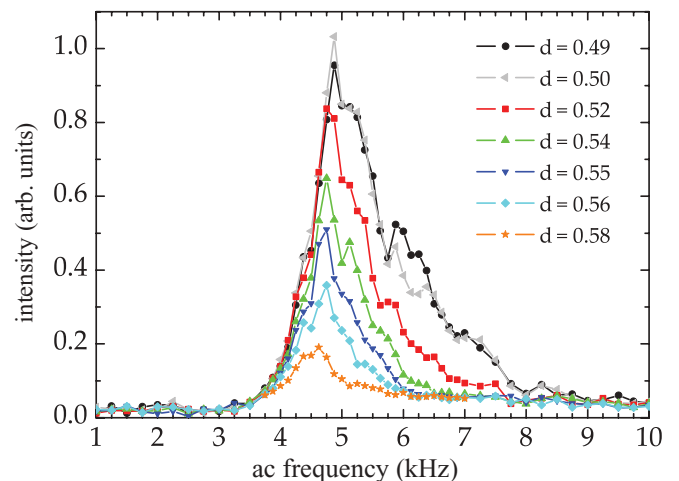


FIG. 9. (Color online) Transmission of 4-aminobenzonitrile for  $d \geq 0.49$  as a function of the ac frequency measured with optimized start phases; see text for details.

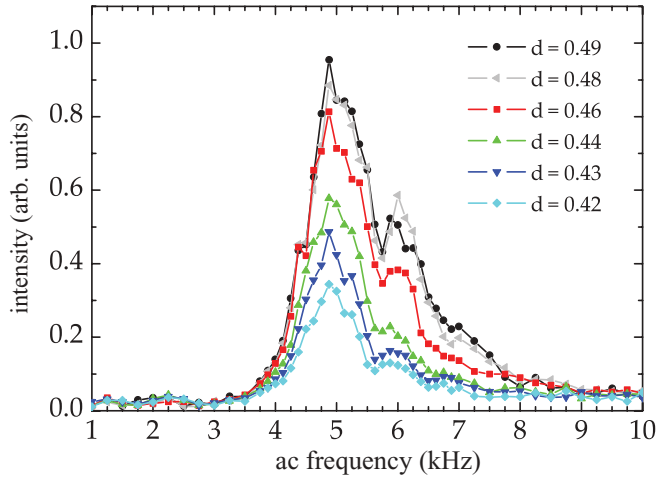


FIG. 10. (Color online) Transmission of 4-aminobenzonitrile for  $d \leq 0.49$  as a function of the ac frequency measured with optimized start phases; see text for details.

The measurements are repeated for  $d < 0.49$  and shown in Fig. 10. The same trend is found as for  $d > 0.49$ . With increasing asymmetry of the switching sequence the width and the peak intensity of the transmission curve both decrease. Figure 11(a) directly compares the transmission curves for  $d > 0.49$  (filled symbols) with the transmission

curves obtained for  $d < 0.49$  (open symbols). Apart from small deviations, the shape of the transmission curve for  $d = 0.54$  corresponds to the curve for  $d = 0.44$ . Similarly, the transmission curve obtained for  $d = 0.56$  resembles the one for  $d = 0.42$ . Figure 11(a) indicates that the transmission characteristics of the selector are symmetric with respect to  $d = 0.49$  rather than to  $d = 0.50$ , as it is theoretically expected (see Fig. 4).

Monte Carlo simulations are performed to simulate the experimental transmission curves and are shown as solid curves together with the experimental data in Fig. 11(b). All simulations have been scaled by a factor of 0.37. The simulations nicely reproduce the low-frequency cutoff and the peak positions of the transmission curves. Assuming that the simulations are symmetric with respect to  $d = 0.50$ , whereas the experiments are symmetric with respect to  $d = 0.49$ , also the relative peak intensities for the different duty cycles can be reproduced. However, similar to previous results for 3-aminophenol [21] and ammonia [36], the simulations overestimate the intensities at the high-frequency side of the maximum and, thereby, the widths of the transmission curves. These differences and the required overall scaling factor might be caused by misalignment of the electrodes, which is not included in the simulations. Such misalignment is known to affect both the overall transmission [18] and the shape of the frequency-dependent transmission curve of an AG focusing device [20]. While the discrepancy between

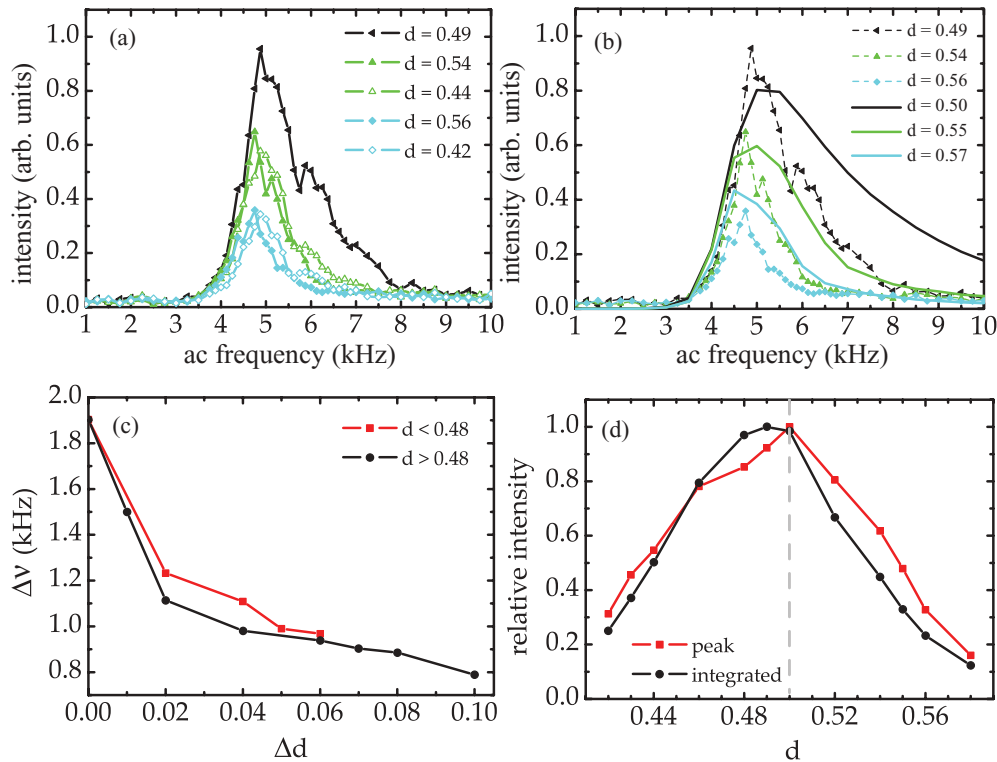


FIG. 11. (Color online) (a) Comparison of transmission curves obtained for  $d < 0.49$  with the curves for  $d > 0.49$ . (b) Comparison of experimental transmission curves (dashed lines with symbols) with simulated transmission curves (solid lines) for an ensemble with  $T_{\text{rot}} = 0.7$  K. The duty cycle for each curve is given in the inset. The experimental transmission curves are symmetric with respect to  $d = 0.49$ , whereas the simulated transmission curves are symmetric with respect to  $d = 0.50$ . All simulations have been scaled by a factor of 0.37. (c) Width (FWHM)  $\Delta\nu$  of the transmission curve as a function of the change of duty cycle  $\Delta d = |0.48 - d|$ . (d) Peak intensity and integrated intensity of the transmission curve as a function of  $d$ . The gray dashed line indicates the theoretically expected maximum at  $d = 0.50$ .

TABLE I. Widths (FWHM)  $\Delta\nu$ , relative widths  $\Delta\nu^{\text{rel}}$ , relative peak intensities  $I_{\text{peak}}^{\text{rel}}$ , relative integrated intensities  $I_{\text{int}}^{\text{rel}}$ , and ac frequencies for maximum intensity  $\nu_{\text{peak}}$  of transmission curves for different duty cycles. Note that the transmission curves were measured in steps of 0.125 kHz and that a more accurate determination of  $\nu_{\text{peak}}$  by interpolation between the data points is difficult for the given shape of the transmission curves (see Figs. 7 and 8).

$d$	$\Delta\nu$ (kHz)	$\Delta\nu^{\text{rel}}$	$I_{\text{peak}}^{\text{rel}}$	$I_{\text{int}}^{\text{rel}}$	$\nu_{\text{peak}}$ (kHz)
0.42	0.97	0.51	0.31	0.25	4.875
0.43	0.99	0.52	0.46	0.37	4.875
0.44	1.11	0.58	0.55	0.50	4.875
0.46	1.23	0.65	0.78	0.79	4.875
0.48	1.90	1.00	0.85	0.97	4.875
0.49	1.50	0.79	0.92	1.00	4.875
0.50	1.11	0.59	1.00	0.98	4.875
0.52	0.98	0.52	0.81	0.67	4.750
0.54	0.94	0.49	0.62	0.45	4.750
0.55	0.90	0.47	0.48	0.33	4.750
0.56	0.89	0.47	0.33	0.23	4.750
0.58	0.79	0.41	0.16	0.12	4.750

experiment and simulation hinders a quantitative comparison of the widths, qualitatively a good agreement on changing the duty cycle is found. For the simulations that are shown in Fig. 11(b) the lowest 400  $J_{K_a K_c} M$  quantum states are included and a rotational temperature of 0.7 K is assumed. This temperature is somewhat lower than previously observed under comparable conditions [34] but not unrealistic given that the lowest literature value of the rotational temperature for similar expansion conditions is 0.4 K (aniline seeded in He [37]). An accurate determination of the rotational temperature by comparison of simulated and experimental transmission curves is difficult because the differences in the shapes are relatively large. However, the position of the low-frequency cutoff is quite sensitive to changes of the rotational temperature and comparing simulations and experiment suggests that  $T_{\text{rot}} \lesssim 1$  K. In order to characterize the properties of the selector in more detail, the FWHM of the transmission curves are calculated. As shown in Fig. 11(c), the widths of the transmission curves are symmetric with respect to  $d = 0.48$ . However, one has to be careful in the determination of the width of the transmission curve, since remaining phase effects influence its value. Note that the transmission curves for  $d = 0.50$ ,  $d = 0.49$ , and  $d = 0.48$  look very similar, even

though the FWHM differs between them (compare Figs. 9 and 10). Despite the possibly inaccurate determination of the exact value of the FWHM, the width of the transmission curve decreases from approximately 1.9 kHz at  $d = 0.48$  to 0.8 kHz at  $d = 0.58$ , demonstrating the improved resolution of the selector that is obtained upon changing the duty cycle. Finally, the peak intensities and the integrated intensities of the transmission curves are plotted as a function of the duty cycle in Fig. 11(d). While the highest peak intensity is observed for  $d = 0.50$  and a frequency of 4.875 kHz, the highest integrated intensity is obtained for  $d = 0.49$ . Taking all criteria, namely shape, width, and intensities of the transmission curves into account, it is concluded that  $d = 0.49$  represents the “optimal” duty cycle for the present setup. This deviation from  $d = 0.50$  is attributed to misalignment of the electrodes. Table I summarizes the characteristics of the transmission curves for the different duty cycles.

## VI. CONCLUSIONS

In this article, we have shown both theoretically and experimentally how the selectivity of an  $m/\mu$  selector, which is based on the AG focusing principle, can be optimized. The selectivity of the selector can be considerably improved by building a longer device, thereby increasing the number of switching cycles. Higher electric field gradients, resulting in a deeper focusing potential, a higher transmission, and higher ac frequencies, will also be beneficial for the performance of a next-generation selector. We are currently setting up such an improved device, implementing an improved mechanical setup to minimize detrimental effects due to misalignment of the electrodes. Just as the availability of quadrupole mass filters with ever higher resolution was crucial for the development of the field of mass spectrometry, pushing the resolution as far as possible will be important for future applications of the  $m/\mu$  selector. This could include the separation of different species, i.e., the isomers of complex (bio-)molecules, including constitutional isomers and conformers, molecular isotopomers, different sizes of atomic or molecular clusters, or even the structural isomers for single cluster sizes.

## ACKNOWLEDGMENTS

We acknowledge the excellent technical support at the Fritz-Haber-Institut. We thank M. R. Tarbutt and H. L. Bethlem for valuable discussions.

- [1] W. Gerlach and O. Stern, *Z. Phys.* **9**, 349 (1922).
- [2] I. I. Rabi, J. R. Zacharias, S. Millman, and P. Kusch, *Phys. Rev.* **53**, 318 (1938).
- [3] J. P. Gordon, H. J. Zeiger, and C. H. Townes, *Phys. Rev.* **95**, 282 (1954).
- [4] H. L. Bethlem, G. Berden, and G. Meijer, *Phys. Rev. Lett.* **83**, 1558 (1999).
- [5] S. Y. T. van de Meerakker, H. L. Bethlem, and G. Meijer, *Nature Phys.* **4**, 595 (2008).
- [6] M. T. Bell and T. P. Softley, *Mol. Phys.* **107**, 99 (2009).
- [7] H. G. Bennewitz, W. Paul, and C. Schlier, *Z. Phys.* **141**, 6 (1955).
- [8] E. D. Courant and H. S. Snyder, *Ann. Phys.* **3**, 1 (1958).
- [9] E. D. Courant, M. S. Livingston, and H. S. Snyder, *Phys. Rev.* **88**, 1190 (1952).
- [10] W. Paul, *Rev. Mod. Phys.* **62**, 531 (1990).
- [11] W. Paul and H. Steinwedel, *Z. Naturforsch. A* **8**, 448 (1953).
- [12] W. Paul, O. Osberghaus, and E. Fischer, *Forschungsberichte des Wirtschafts- und Verkehrsministeriums Nordrhein-Westfalen*, Vol. 415 (Westdeutscher Verlag, Germany, 1958).
- [13] D. Auerbach, E. E. A. Bromberg, and L. Wharton, *J. Chem. Phys.* **45**, 2160 (1966).

- [14] D. Kakati and D. C. Lainé, *Phys. Lett. A* **24**, 676 (1967).
- [15] H. L. Bethlem, A. J. A. van Roij, R. T. Jongma, and G. Meijer, *Phys. Rev. Lett.* **88**, 133003 (2002).
- [16] H. L. Bethlem, M. R. Tarbutt, J. Küpper, D. Carty, K. Wohlfart, E. A. Hinds, and G. Meijer, *J. Phys. B* **39**, R263 (2006).
- [17] M. R. Tarbutt, H. L. Bethlem, J. J. Hudson, V. L. Ryabov, V. A. Ryzhov, B. E. Sauer, G. Meijer, and E. A. Hinds, *Phys. Rev. Lett.* **92**, 173002 (2004).
- [18] K. Wohlfart, F. Grätz, F. Filsinger, H. Haak, G. Meijer, and J. Küpper, *Phys. Rev. A* **77**, 031404(R) (2008).
- [19] T. Junglen, T. Rieger, S. A. Rangwala, P. W. H. Pinkse, and G. Rempe, *Phys. Rev. Lett.* **92**, 223001 (2004).
- [20] T. E. Wall, S. Armitage, J. J. Hudson, B. E. Sauer, J. M. Dyne, E. A. Hinds, and M. R. Tarbutt, *Phys. Rev. A* **80**, 043407 (2009).
- [21] F. Filsinger, U. Erlekam, G. von Helden, J. Küpper, and G. Meijer, *Phys. Rev. Lett.* **100**, 133003 (2008).
- [22] L. Holmegaard, J. H. Nielsen, I. Nevo, H. Stapelfeldt, F. Filsinger, J. Küpper, and G. Meijer, *Phys. Rev. Lett.* **102**, 023001 (2009).
- [23] F. Filsinger, J. Küpper, G. Meijer, J. L. Hansen, J. Maurer, J. H. Nielsen, L. Holmegaard, and H. Stapelfeldt, *Angew. Chem. Int. Ed.* **48**, 6900 (2009).
- [24] M. Hillenkamp, S. Keinan, and U. Even, *J. Chem. Phys.* **118**, 8699 (2003).
- [25] G. Berden, J. van Rooy, W. L. Meerts, and K. A. Zachariasse, *Chem. Phys. Lett.* **278**, 373 (1997).
- [26] J. A. Richards, R. M. Huey, and J. Hiller, in *Proceedings of the Institution of Radio and Electronics Engineers, Australia* (Institution of Radio and Electronics Engineers, Sydney, Australia, 1971), Vol. 32, pp. 321–322.
- [27] J. A. Richards, R. M. Huey, and J. Hiller, *Int. J. Mass Spectrom. Ion Processes* **12**, 317 (1973).
- [28] N. Kononkov, M. Sudakov, and D. Douglas, *J. Am. Soc. Mass. Spectrom.* **13**, 597 (2002).
- [29] L. A. Pipes, *J. Appl. Phys.* **24**, 902 (1953).
- [30] A. Osterwalder, S. A. Meek, G. Hammer, H. Haak, and G. Meijer, *Phys. Rev. A* **81**, 051401(R) (2010).
- [31] P. Lützow, M. Schnell, and G. Meijer, *Phys. Rev. A* **77**, 063402 (2008).
- [32] W. Paul and M. Raether, *Z. Phys.* **140**, 262 (1955).
- [33] J. Küpper and F. Filsinger, libcoldmol: A particle trajectory calculation framework (2003–2008) [<http://libcoldmol.cold-molecules.info>].
- [34] F. Filsinger, J. Küpper, G. Meijer, L. Holmegaard, J. H. Nielsen, I. Nevo, J. L. Hansen, and H. Stapelfeldt, *J. Chem. Phys.* **131**, 064309 (2009).
- [35] D. R. Borst, T. M. Korter, and D. W. Pratt, *Chem. Phys. Lett.* **350**, 485 (2001).
- [36] J. Küpper, F. Filsinger, and G. Meijer, *Faraday Discuss.* **142**, 155 (2009).
- [37] U. Even, J. Jortner, D. Noy, N. Lavie, and N. Cossart-Magos, *J. Chem. Phys.* **112**, 8068 (2000).